MNRAS **000**, 1–15 (2016) Preprint 24 November 2016 Compiled using MNRAS LATEX style file v3.0

A closer look at the "characteristic" width of molecular cloud filaments

G. V. Panopoulou,[1,2]⋆ I. Psaradaki,[1] R. Skalidis, [1] K. Tassis,[1,2] J. J. Andrews[2]
[1] *Department of Physics and ITCP†, University of Crete, 71003, Heraklion, Greece*
[2] *Foundation for Research and Technology - Hellas, IESL, Voutes, 71110 Heraklion, Greece*

arXiv:1611.07532v1 [astro-ph.GA] 22 Nov 2016

Accepted 2016 November 22. Received 2016 November 22; in original form 2016 September 13

ABSTRACT

Filaments in *Herschel* molecular cloud images are found to exhibit a "characteristic width". This finding is in tension with spatial power spectra of the data, which show no indication of this characteristic scale. We demonstrate that this discrepancy is a result of the methodology adopted for measuring filament widths. First, we perform the previously used analysis technique on artificial scale-free data, and obtain a peaked width distribution of filament-like structures. Next, we repeat the analysis on three *Herschel* maps and reproduce the narrow distribution of widths found in previous studies − when considering the average width of each filament. However, the distribution of widths measured at all points along a filament spine is broader than the distribution of mean filament widths, indicating that the narrow spread (interpreted as a "characteristic" width) results from averaging. Furthermore, the width is found to vary significantly from one end of a filament to the other. Therefore, the previously identified peak at 0.1 pc cannot be understood as representing the typical width of filaments. We find an alternative explanation by modelling the observed width distribution as a truncated power-law distribution, sampled with uncertainties. The position of the peak is connected to the lower truncation scale and is likely set by the choice of parameters used in measuring filament widths. We conclude that a "characteristic" width of filaments is not supported by the available data.

Key words: ISM: structure – ISM: clouds – stars: formation – submillimetre: ISM – methods: statistical – ISM: individual objects: Polaris Flare, Aquila Rift, IC 5146

1 INTRODUCTION

Studies of the structure of molecular clouds can provide clues on how gas accumulates to form stars. Gas in molecular clouds is found to be ordered in filamentary structures, a result highlighted especially by *Herschel* observations of dust emission in nearby clouds (André et al. 2010). Dense, self-gravitating filaments are often found to be co-spatial with young stars and dense prestellar cores (e.g. Hartmann 2002; André et al. 2010; Polychroni et al. 2013; Könyves et al. 2015), and hence may be important for understanding star formation.

One of the most striking results from analyses of *Herschel* data is that filaments in the Gould Belt clouds are found to exhibit a narrow distribution of average cross-sectional widths[1] (Arzoumanian et al. 2011). This sharply peaked distribution (with a mean at ∼ 0.1 pc and with ∼ 70% of values within 0.06−0.14 pc, Arzoumanian et al. 2011; Koch & Rosolowsky 2015) contains filaments spanning more than two orders of magnitude in column density.

This finding seems to contradict the expectation that filaments should contract (due to gravity) and hence increase in density while decreasing in radius. Though the existence of this characteristic scale is still poorly understood, it has been suggested that it must be connected to some physical mechanism, perhaps one involved in filament formation (Arzoumanian et al. 2011; André et al. 2014). Qualitative arguments have connected this characteristic scale to the transition from supersonic to trans-sonic turbulence (Arzoumanian et al. 2011) and to the ambipolar diffusion length scale (for both gravitationally unbound and bound structures Hennebelle 2013; Hennebelle & André 2013). Simple analytical models propose that the independence of filament

⋆ E-mail: panopg@physics.uoc.gr
† Institute for Theoretical and Computational Physics, formerly Institute for Plasma Physics

[1] Throughout this paper the term 'width' refers to the FWHM of a Gaussian fit to the inner-most part of a filament radial profile, the same definition used by Arzoumanian et al. (2011).

© 2016 The Authors

width from column density may be a result of the balance between accretion onto the (self-gravitating) filaments and dissipation of the turbulence within them (Hennebelle & André 2013; Heitsch 2013). Fischera & Martin (2012) offered pressure confinement of isothermal cylinders as a possible model for self-gravitating filaments. Most recently, Auddy, Basu & Kudoh (2016) proposed a model in which filaments are magnetic ribbons, produced by large-scale, trans-Alfvénic turbulent flows in a strong magnetic field. Their model is able to reproduce average widths that vary within a factor of two across two orders of magnitude in column density. However, simulations which either include self-gravity and neglect magnetic fields or vice versa have yet to reproduce the observed distribution and independence on column density (Smith, Glover & Klessen 2014; Ntormousi et al. 2016). Federrath (2016) simulated isothermal, self-gravitating, magnetized clouds with super-Alfvénic driven turbulence. His finding is that filament widths are peaked at 0.1 pc and appear constant for one order of magnitude in column density, when turbulence is operating. The proposed explanation is that the characteristic width is set by the dissipation of turbulence in shocks. His model, however, fails to reproduce the correlation between filament and magnetic field orientations found in molecular clouds with *Planck* (Planck Collaboration Int. XXXV 2016).

One particularly puzzling observation regarding the apparent characteristic width of filaments is the absence of its imprint on the spatial power spectra of *Herschel* cloud images (Miville-Deschênes et al. 2016). The spatial power spectrum of the 250 μm map of the translucent non-star-forming Polaris Flare is well fit by a power law from ~ 2 pc to ~ 0.02 pc (Miville-Deschênes et al. 2010). At the same time, the distribution of filament widths in this cloud is found to have a prominent peak at $0.05 - 0.07$ pc (Arzoumanian et al. 2011; Panopoulou, Psaradaki & Tassis 2016). A similar situation is found in the Chamaeleon molecular cloud complex, where filament widths are peaked around 0.12 pc with a spread of 0.04 pc (Alves de Oliveira et al. 2014). However, these authors find no indication of a typical filament width in the Δ-variance spectra (Stutzki et al. 1998) of the clouds, even though the signature of cores and clumps is easily identified as a change in the slope of the Δ-variance spectrum at the corresponding size scales.

Motivated by this apparent discrepancy, in this work we retrace the steps in the analyses of filament width distributions. In section 2, we briefly describe the analysis used for constructing the distribution of filament widths. We first perform this analysis on an artificial filamentary image with no characteristic scale and find the distribution of widths to have a broad peak (section 3.1). We then repeat the analysis on *Herschel* data of three clouds (the Polaris Flare, Aquila and IC 5146, section 3.2), showing that the narrow spread of the distribution of widths found in previous studies is likely a consequence of averaging along filaments. The constancy of filament widths may therefore not be inferred from this spread. Furthermore, we investigate the position of the peak of the distribution of widths and find that it is likely a result of the choice of range within which the filament width has been measured (section 3.3). Finally, we summarize our results in section 4.

2 METHODS

In order to reproduce the distributions of filament widths for the three clouds presented in Arzoumanian et al. (2011) (the Polaris Flare, Aquila, and IC 5146), we follow an analysis similar to their study. We use primarily the *Herschel* Spectral and Photometric Imaging Receiver (SPIRE) maps of these clouds at 250 μm, unless explicitly stated otherwise in the text.

First, we employ the Discrete Persistent Structures Extractor (`DISPERSE`, Sousbie 2011), to identify the filamentary structures in each image. `DISPERSE` analyses the topology of a given map and extracts its skeleton, which corresponds to the ridges of elongated structures. We select the parameters of `DISPERSE` so that the resulting skeletons are visually similar to those shown in the previous studies of the three clouds (Arzoumanian et al. 2011, IC 5146, figure 3), (Könyves et al. 2015, Aquila, figure 3), (André et al. 2014, Polaris Flare, figure 1). The values of the parameters used are given in appendix A.

Next, we provide the skeleton of `DISPERSE` and the corresponding *Herschel* image of each cloud as input to the Filament Trait-Evaluated Reconstruction (`FILTER`) code[2] (Panopoulou et al. 2014). The objective of `FILTER` is twofold: First, it post-processes the skeleton of `DISPERSE` to only include continuous, non-spurious, structures (e.g. peaked well above the noise level). This is done by taking cross-sections at every pixel along the filament ridge and assessing each intensity profile. Profiles that are not peaked around the filament ridge and above the noise-level are rejected. Second, `FILTER` measures the width of each intensity profile along a filament. The width is defined as the FWHM of a Gaussian fit (with offset) to the inner-most part of the profile (as in Arzoumanian et al. 2011). In order to find this value automatically for every profile, Gaussians are fit iteratively to smaller and smaller distances from the filament ridge. The initial range used for fitting is a free parameter of the algorithm. As has been shown by Smith, Glover & Klessen (2014), the distance up to which a Gaussian is fit is crucial in the determination of the width, as at larger distances the fit tends to miss the inner-most part of the profile. In each section we shall state explicitly which starting value for the fitting range has been used. At the end of the iteration, the most frequent FWHM is assigned as the width of the profile, after deconvolution from the beam size[3]. The deconvolved width is found (as in Könyves et al. 2015) by $\mathrm{FWHM_d} = \sqrt{\mathrm{FWHM}^2 - \mathrm{HPBW}^2}$, where HPBW is the half-power beam width of the map ($18''$for 250 μm, which corresponds to 0.013 pc, 0.023 pc, and 0.04 pc at the assumed distances to the Polaris Flare, 150 pc, Aquila, 260 pc, and IC 5146, 460 pc, respectively). Finally, only sufficiently elongated structures (with at least a 3:1 length to mean width ratio) are included in the final sample of filaments that we consider for further analysis. The post-processed skeletons of the three *Herschel* images used in this work are shown in appendix A.

[2] The code is available at: `https://bitbucket.org/ginpan/filter`
[3] The most frequent FWHM has been found through tests (on data and artificial images) during code development to be a robust estimator of the width.

FILTER provides two different ways of constructing width distributions:

i. A distribution of the FWHM measured at all points along the spines of filaments can be created. Information on the structure to which each measurement belongs is discarded in this way (e.g. Panopoulou, Psaradaki & Tassis 2016). We refer to this kind of distribution as the distribution of all profile widths.
ii. A distribution of the mean FWHM of filaments can be constructed. This second type of distribution has been found to show a "characteristic width" in previous studies (e.g. Arzoumanian et al. 2011). We refer to this type of distribution as the distribution of filament-averaged widths (or of mean filament widths).

With FILTER the mean width of each filament is found by taking the average value of the FWHM measured at each point (pixel) along the filament ridge. In other studies, the mean width has been found by fitting a Gaussian to the mean filament profile e.g. Arzoumanian et al. (2011); Koch & Rosolowsky (2015); Smith, Glover & Klessen (2014); Benedettini et al. (2015). In the work of Koch & Rosolowsky (2015), a non-parametric width determination is also used when Gaussian fitting is not possible. In the following analysis we find the mean width of a filament by averaging the FWHM of all its profiles, as this process is automated, objective, and easily reproducible. We note that the method used to calculate the average width of a filament should not affect the statistical properties of the distribution of mean filament widths (mean and spread), as long as a large number of filaments is used. Indeed, the difference between our approach of measuring mean filament widths and that of other studies does not affect the properties of the distributions of mean filament widths, as both the mean and spread are in good agreement with those of Arzoumanian et al. (2011) (section 3.2).

3 RESULTS

3.1 Can a peaked size distribution arise from scale-free data?

The scale-free spatial power spectrum of the *Herschel* Polaris Flare image (at 250 μm) is in tension with the existence of a "characteristic" width of the filaments in the same image (Miville-Deschênes et al. 2010; Arzoumanian et al. 2011). It may be argued that in some circumstances, the imprint of a characteristic scale on the spatial power spectrum is "hidden". We use simple artificial images to explore if such a situation may arise, in appendix B. We demonstrate that if structures with a characteristic scale are introduced, an imprint of this scale is apparent in the spatial power spectrum – as long as the structures are easily discernible from background noise, as is the case for filaments in the Polaris Flare.

In this section we explore the opposite situation: whether a preferred scale can arise from analysing an image with a scale-free spatial power spectrum. To this end, we create a scale-free image and perform the analysis described in section 2.

To construct the image we use the Ridged Multifractal model from the suite of noise-synthesis models implemented in the python library pynoise (http://pynoise.readthedocs.io). Noise synthesis models (Musgrave, Kolb & Mace 1989) are used for creating natural-looking complex and heterogenous patterns (landscapes, clouds). They are based on the widely used, scale-free, fractional-Brownian-motion (fBm) (e.g. Stutzki et al. 1998) but use band-limited Perlin noise (Perlin 1985) functions for the basis function instead of sine waves as in pure fBm.

The resulting image (256 pixels on each side) is filamentary, as can be seen in Fig. 1 (left). We adjusted the parameters of the model to obtain an image whose spatial (azimuthally-averaged) power spectrum has the form of a power law (Fig. 1 - top right). The one dimensional spatial power spectrum is constructed as in Pingel et al. (2013), by taking the median power in concentric annuli around the zero-frequency pixel in the two-dimensional power spectrum. The annuli are chosen so that a uniform sampling of scales in logarithmic space is obtained. The sample size ranges from 29 (for the smallest annulus) to ∼23000 values. The errors on the median value (comparable to the size of the points in the figure) are calculated by bootstrap resampling. For every annulus, we resample the distribution of intensities and calculate the median of the resampled distribution 100 times. The error on the median is the standard deviation of these 100 median values.

We performed the analysis described in section 2 on the artificial image. The resulting skeletons of filament-like structures (having at least a 3:1 aspect ratio) are overplotted in the left panel of Fig. 1. The distribution of widths measured at each point along these elongated structures (first method) is shown in the bottom right panel of Fig. 1. The initial fitting range used is ±10 pixels from the ridge (see discussion in section 2 regarding the fitting range). The distribution is clearly peaked around 12 pixels, and has a spread of 3.8 pixels.

The existence of a peak in the distribution of widths of the structures extracted by DISPERSE in this image is inconsistent with its scale-free (power-law) spatial power spectrum. Since the construction of the power spectrum is straight-forward, we conclude that the existence of the preferred scale (peak of the width distribution) is most likely an artefact of the analysis of apparent filament widths.

3.2 Why is the distribution of widths narrow?

We now turn to the *Herschel* data of the Polaris Flare, Aquila, and IC 5146. When combining width measurements of filaments in these clouds, Arzoumanian et al. (2011) find a distribution of mean filament widths with a spread of only 0.03 pc. It is this small spread that seems to imply that filaments have a "characteristic width". In this section, we attempt to understand why the distribution of widths is found to have such a narrow spread.

We follow the analysis of section 2 on the *Herschel* SPIRE-250 μm map of each cloud. We construct the distribution of widths measured at every cross-section (profile) of the filaments in the map. Studies finding a "characteristic width" have used the width of the mean profile of individual filaments to create the distribution of (mean filament) widths (e.g. by fitting a Gaussian to the mean filament profile, Arzoumanian et al. 2011). For comparison, we also con-

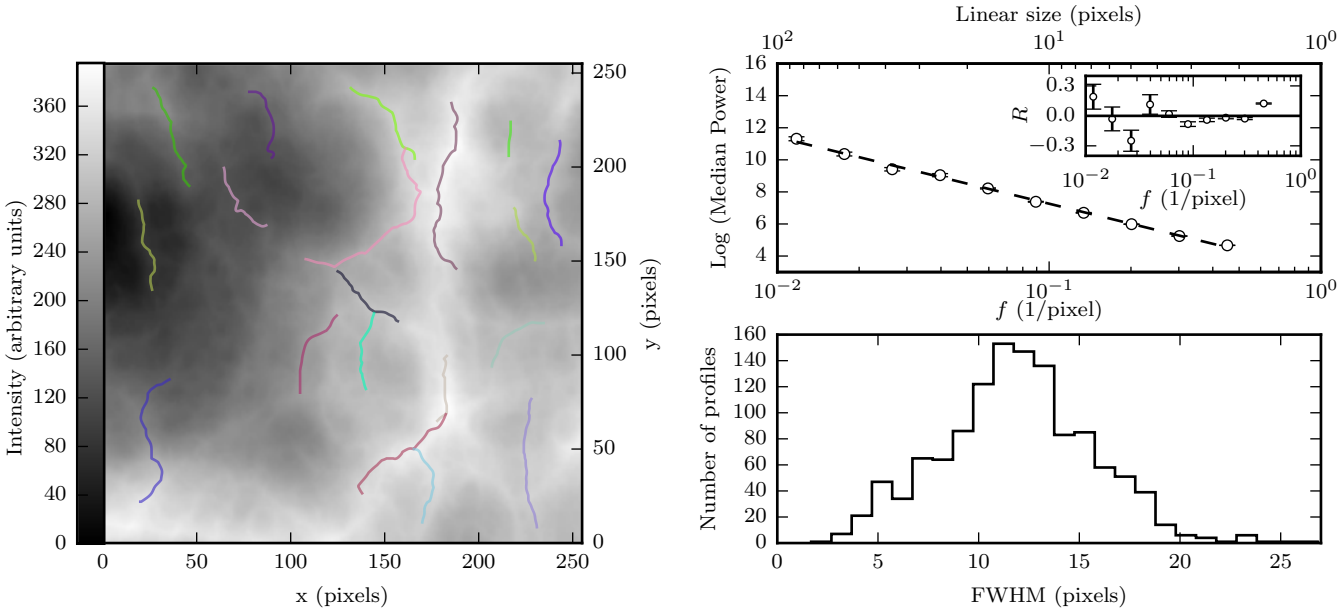

Figure 1. Left: Image generated using Ridged Multifractal Noise (256 pixels on each side), with the skeleton of filaments having an aspect ratio of at least 3:1 overplotted. Top right: Spatial (azimuthally-averaged) power spectrum of image on left (open circles) and linear fit in log-log space (dashed line). Corner inset: Residual of the fit, R = log(median power) - log(fit). Bottom right: Distribution of the widths measured at each point along the ridges of the filaments in the artificial image on the left.

Table 1. Properties of width distributions shown in Fig. 2. Includes the number of filaments in each distribution, N_{fil}, the number of profiles of all filaments, N_{pr}, the mean and standard deviation of the distribution of filament-averaged widths ($\langle W_{mean} \rangle$ and σ_{mean}), and those of the distribution of all profile widths ($\langle W_{all} \rangle$, σ_{all}).

Cloud	N_{fil}	N_{pr}	$\langle W_{mean} \rangle$ (pc)	$\langle W_{all} \rangle$ (pc)	σ_{mean} (pc)	σ_{all} (pc)
Polaris	100	24969	0.095	0.097	0.014	0.05
Aquila	79	14315	0.095	0.094	0.02	0.04
IC 5146	58	5277	0.11	0.11	0.02	0.04
All	237	44561	0.09	0.09	0.02	0.04

struct the distribution of mean filament widths (as explained in section 2).

In Fig. 2 we show the normalized distribution of filament-averaged widths (dotted) and that of all profile widths (solid), for each of the clouds mentioned above. The number of filaments used to create these distributions as well as the mean and spread of the distributions are shown in Table 1. The initial fitting range used for all distributions was ±0.1 pc from the filament ridge. We find that the mean and spread of the distribution of mean filament widths for the filaments in IC 5146, and for those in all three clouds combined are in agreement with those found by Arzoumanian et al. (2011) (the reported mean and spread were 0.1 pc and 0.03 pc, respectively).

When comparing the distribution of all filament profiles to that of mean widths we find that *the shapes of the two kinds of distribution are clearly different.* The filament-averaged width distribution is much more concentrated around its mean value ($\sigma_{all} \approx [2-3] \times \sigma_{mean}$, from Table 1), and lacks the tails seen in the width distribution of all profiles. The same effect is seen when filaments from all clouds are combined in a single distribution (bottom panel, Fig. 2).

The differences between the two kinds of distributions can be easily understood considering the Central Limit Theorem (CLT). The average value of a sample of profile widths (filament) is expected to follow a Gaussian distribution, provided there is a sufficient number of filaments and that widths are not strongly correlated within a filament. This distribution of averages is centred around the mean of the parent distribution (that containing the widths of all filament profiles). It is therefore not surprising that the spread in the distribution of filament-averaged widths is small. The information conveyed by the narrowness of this distribution is simply that the *mean width of filaments is known with very good accuracy; not that the widths of individual filaments are constant*, as has often been interpreted.

We now wish to understand the factors that determine the spread of the distribution of mean filament widths (i.e. we wish to find the parameters P that enter in $\sigma_{mean} = f(P)$). From the original form of the CLT (which assumes measurements are completely uncorrelated), we expect that

$$\sigma_{mean} = \sigma_{all}/\sqrt{N}, \quad (1)$$

if all filaments have the same number of profiles N (which is proportional to the filament length). However, the lengths of filaments follow a distribution of values $g(N)$, and therefore we expect $\sigma_{mean} = f(\sigma_{all}, g(N))$.

In order to test whether these two parameters are sufficient to explain the observed σ_{mean} in the Polaris Flare,

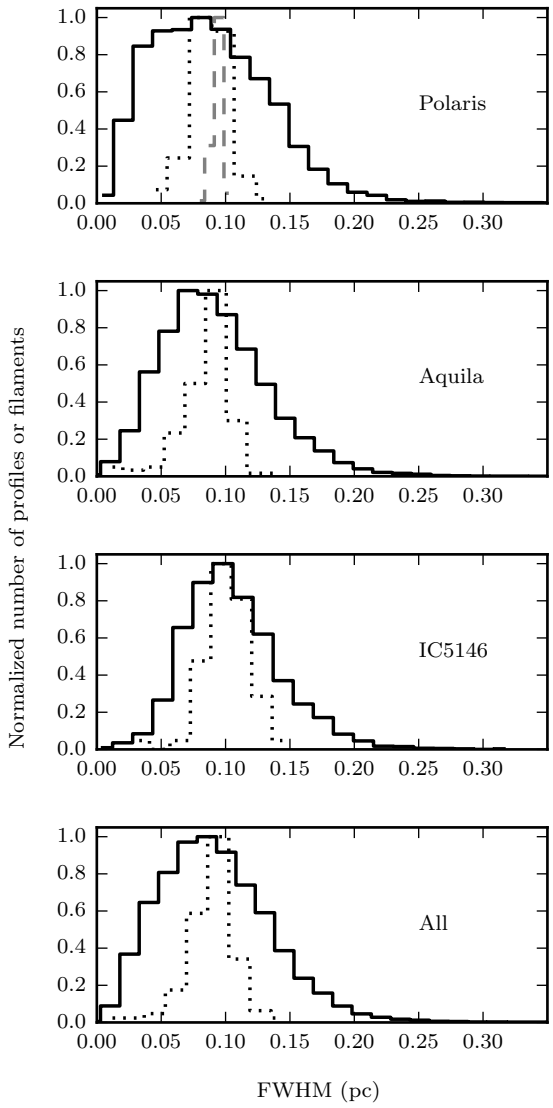

Figure 2. Comparison of filament-averaged (dotted) and non-averaged (solid black) width distributions for the three different clouds (top 3 plots), and for all filaments in the three clouds combined (bottom). All FWHM have been deconvolved from the beam size. The grey dashed line (top panel) shows the distribution of mean filament widths resulting from the Monte Carlo simulation described in the text (section 3.2).

we attempt to reproduce the distribution of mean filament widths from that of all profile widths as follows. We perform a Monte Carlo simulation where samples of widths are drawn randomly from the observed distribution of all profile widths. These samples are randomly assigned to 100 groups (or fake 'filaments'), corresponding to the 100 filaments found in the Polaris Flare. The size of each group (corresponding to the length of the 'filament') is drawn from the observed distribution of filament lengths. We then calculate the average width of each group and construct the distribution of group-averaged widths. This process produces a distribution with $\sigma_{mean}^{rand} = 0.004$ pc, much narrower than what is observed (see grey dashed distribution at the top panel of Fig. 2).

The information that is lacking is that widths within the telescope beam size are strongly correlated. We provide evidence for this by constructing the Autocorrelation Function of widths along the ridge of filaments, in appendix C. By performing a simulation similar to that described above, including this final piece of information, we are able to reproduce the observed spread of the distribution of mean widths ($\sigma_{mean} = 0.011$ pc, see appendix C). Therefore, the parameters that most significantly affect σ_{mean} can be summarized as: $\sigma_{mean} = f(\sigma_{all}, g(N), beam)$. In other words, *there is no other information to be extracted from the spread of the filament-averaged width distribution.*

Since the structure of individual filaments cannot be inferred uniquely from their average properties, we must examine how much does the width throughout an entire filament vary. This question can be answered by considering the standard deviation of all widths measured at different positions along the spine of a filament. Individual filaments are known to exhibit a range of FWHM along their spines ($0.1-1$ pc, $0.07-0.2$ pc, $0.1-2.5$ pc Juvela et al. 2012; Malinen et al. 2012; André et al. 2016). In the Polaris Flare, the standard deviation of profile widths in a given filament is on average $\langle\sigma_{fil}\rangle = 0.04$ pc. This value is similar to the spread of the parent width distribution ($\sigma_{all} = 0.05$ pc, Table 1). *Therefore, the width varies significantly throughout the entire extent (length) of an individual filament.* This finding is also supported by the two-dimensional distribution of filament widths across the Polaris Flare map, presented in Panopoulou, Psaradaki & Tassis (2016) – their figure 7. Filament widths do not exhibit large-scale regularities, but rather fluctuate in a seemingly random manner throughout the cloud.

3.3 Why is the peak of the distribution of filament widths at 0.1 pc?

The findings of section 3.2 along with the scale-free power spectrum of the Polaris Flare, render the existence of a "characteristic" width of filaments highly unlikely. Consequently, the previously reported peak of the filament-averaged width distribution at 0.1 pc cannot be explained by such a view.

In order to understand the origin and position of this peak, we examine in detail the width distribution of all filament profiles in the Polaris Flare. Fig. 3 shows the distribution of log(width) with equally-sized bins in logarithmic space. It is strongly peaked and the mean and median values (vertical solid and dotted lines, respectively) differ by only 5×10^{-3} pc. Interestingly, the part of the distribution at scales larger than the mean resembles a straight line (in logarithmic space). A linear fit (in log-log space) to the distribution is shown with a grey solid line in Fig. 3.

This resemblance of part of the distribution to a power-law is not surprising if we consider the evidence for scale-free, or self-similar, structures in the ISM within a range of scales (e.g. Stutzki et al. 1998; Elmegreen & Scalo 2004; Tassis 2007; Elia et al. 2014; Miville-Deschênes et al. 2016). Elmegreen & Falgarone (1996) find size and mass distributions in clouds consistent with those arising from a fractal. In the case of the Polaris Flare, the scale-free nature of the cloud is evidenced by its power-law spatial power spectrum

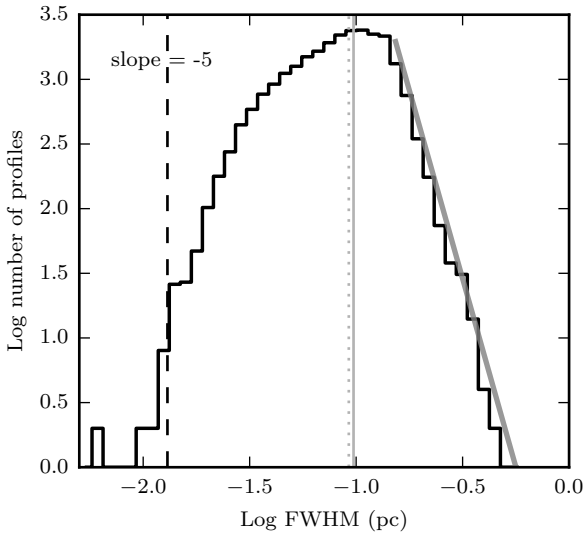

Figure 3. Distribution of the logarithm of all profile widths of filaments in the Polaris Flare. At scales larger than 0.15 pc, the distribution resembles a power law (the grey solid line is a linear fit in log-log space to the logarithmically-spaced bins). The mean and median of the distribution are shown by the vertical solid and dotted lines, respectively. The *Herschel*-SPIRE beam size (at 250 μm) at the distance of the Polaris Flare (150 pc) is shown with the dashed vertical line.

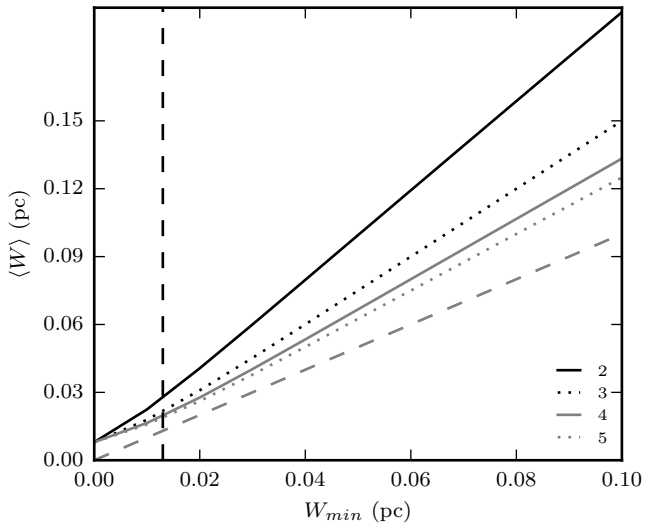

Figure 4. Dependence of the mean measured width of profiles on W_{min} for different values of γ (ranging from 2 to 5 and marked with labelled lines). Values of $W_{max} = 5$ pc and $\sigma = 0.02$ pc were used, since there is little dependence of $\langle W \rangle$ on these parameters (see text). A 1−1 correlation is shown with the dashed grey line. The dashed vertical line shows the *Herschel*-SPIRE beam size (at 250 μm) in parsecs at the distance to the Polaris Flare (150 pc).

(Miville-Deschênes et al. 2010). We note that because the Polaris Flare is gravitationally unbound and is not forming stars (Heithausen 2002; Ward-Thompson et al. 2010; Wagle et al. 2015), self-similarity is not expected to break down at the typical scale of prestellar cores (0.1 pc, e.g. Goodman et al. 1998). Therefore, a power-law distribution of filament widths (in accordance to other length scales) within some range of scales, is not unreasonable.

If a power law size (width) distribution is intrinsic to the cloud, we expect that this power law will be truncated at large scales at a fraction of the size of the *Herschel* map and at small scales (at least) by the resolution. In the process of imaging the cloud dust emission and measuring sizes on the map, errors are introduced. Errors have the effect of smoothing the distribution near the lower truncation limit (Koen & Kondlo 2009). If these errors are assumed Gaussian, then the shape of the (truncated) power law distribution can be analytically modelled (Koen & Kondlo 2009) and is similar to that of the distribution in Fig. 3: it possesses a peak near the lower truncation limit followed by a power law tail. The analytical form of the distribution of measured widths (W) is:

$$f(W) = \int_{W_{min}}^{W_{max}} \frac{\gamma w^{-(\gamma+1)}}{\sqrt{2\pi}\sigma(W_{min}^{-\gamma} - W_{max}^{-\gamma})} \exp\left[-\frac{1}{2}\left(\frac{W-w}{\sigma}\right)^2\right] dw, \quad (2)$$

where w is the width before introducing measurement errors, σ is the measurement uncertainty, $\gamma + 1$ is the power law slope, and W_{min}, W_{max} are the sizes at which the power law is truncated due to (at least) the resolution and (at most) the map size. For what follows, we will consider only non-negative values of γ. The average value can be obtained by (numerical) integration of the formula:

$$\langle W \rangle = \int_{\mathrm{HPBW}}^{\mathrm{map\ size}} f(W) W dW, \quad (3)$$

where the integration is performed within the bounds set by the observations (resolution limit and map size).

Therefore, if one could determine the parameters σ, γ, W_{min}, and W_{max}, a prediction for the mean of the distribution of all profile widths could be obtained. In section 3.2 we found that *the mean of the distribution of all profile widths is coincident with the position of the peak of the filament-averaged distribution (as a result of the CLT). Consequently, measuring the mean of the former kind of distribution determines the peak of the latter.* We note that the mean and peak of the distribution of filament-averaged widths are the same, as it is (approximately) Gaussian.

In Fig. 4 we explore the dependence of $\langle W \rangle$ on the parameters W_{min} and γ. $\langle W \rangle$ is plotted against W_{min} for $W_{max} = 5$ pc, $\sigma = 0.02$ pc, and different values of γ (ranging from 2−5, around a value of 4 implied by the slope of Fig. 3, and marked with solid and dotted lines). We find that there is no dependence of $\langle W \rangle$ on W_{max}. For γ in the range 2−5, constant W_{min} and σ, and W_{max} in the range 1 − 50 pc, $\langle W \rangle$ varies by less than 0.01 pc. Similarly, for constant W_{min} and W_{max}, and σ in the range 0.01−0.1 pc, $\langle W \rangle$ varies by less than 0.02 pc for any given γ within 2−5. On the contrary, $\langle W \rangle$ is very sensitive to the parameter W_{min}. *Therefore, the lower scale at which a power law width distribution is truncated essentially sets the position of the peak in the distribution of filament-averaged widths.*

We would like to identify the best fit parameters for the

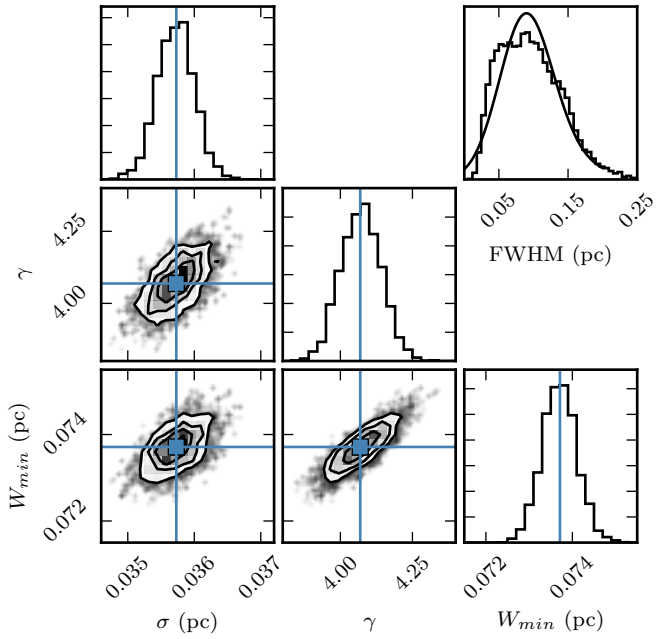

Figure 5. The posterior distribution of parameters from our MCMC model of the data of Fig. 3. Blue lines show the values returned by the MLE. On diagonal: One-dimensional histograms of model parameters: σ, γ, and W_{min}. Lower diagonal: Joint PDFs of the posterior distribution of the model parameters. Top right: comparison between normalized distribution of Fig. 3 (stepped histogram) with our model (equation 2), using a randomly selected set of parameter values from the posterior distribution of model parameters (smooth line).

distribution of filament widths in the Polaris Flare, using a power law with measurement uncertainties. Koen & Kondlo (2009) provide the log-likelihood function for this model:

$$\mathcal{L} = -\frac{N}{2}\log 2\pi - N\log\sigma + N\log\gamma - N\log(W_{min}^{-\gamma} - W_{max}^{-\gamma}) + \sum_{j=1}^{N}\log\int_{W_{min}}^{W_{max}} x^{-(\gamma+1)}\exp\left[-\frac{1}{2}\left(\frac{W_j - x}{\sigma}\right)^2\right]dx \quad (4)$$

where W_j are the N different filament width measurements and σ is the Gaussian standard deviation on measurements of W_j (and is independent from W_j). Since, for the distributions of filament widths, the effect of W_{max} is insignificant, we set it to 10 pc (approximate size of the *Herschel* map) and solve for the best-fit values of W_{min}, γ, and the measurement uncertainty, σ. We use the routine `minimize` within the `scipy.optimize` package, to find the values that maximize the log-likelihood. The resulting values for the parameters are: $\sigma = 0.036$ pc, $\gamma = 4.07$, and $W_{min} = 0.074$ pc. We note that the slope found by fitting a line to the distribution in Fig. 3 (slope = 5) is in good agreement with the value found by maximizing the log-likelihood ($\gamma + 1 = 5.07$). By substituting γ and W_{min} in equation 3, we obtain $\langle W\rangle = 0.098$ pc, which is approximately equal to the mean of the observed distribution of widths.

Additionally, we would like to determine the range of parameter values implied by the filament width data. Instead of using a maximum likelihood estimate (MLE), we use the Markov Chain Monte Carlo (MCMC) algorithm `emcee` (Foreman-Mackey et al. 2013). `emcee` employs an affine-invariant ensemble sampler to probe the model parameter space. Our model uses 32 walkers to maximize the log-likelihood function in Equation 4. We apply flat priors on W_{min} and γ, in the ranges: W_{min}: [0−0.5] pc, γ: [0.01−10]. We use the Jeffreys prior $(1/\sigma)$ on σ to make it scale-invariant. The range used for σ is [0−3] pc. We note that σ encapsulates the uncertainty introduced by two different processes: the imaging of the cloud (resolution) and the measurement of the width (analysis in section 2). We therefore choose to leave σ as a free parameter (and do not set it equal to the image resolution) to account for both sources of error. 200 steps are sufficient for the "burn-in" stage. We throw these data away, and run our model for 2000 additional steps to produce the posterior distribution.

The posterior distributions of model parameters (Fig. 5 − on diagonal) are strongly peaked, with standard deviations of 3×10^{-4} pc for σ, 0.07 for γ, and 4×10^{-4} pc for W_{min}. Joint PDFs of the posterior distributions of model parameters are shown in the panels lower than the diagonal. As expected for uniform priors (and since our prior on σ is weak), the region of high probability parameter space agrees with the results from the maximum likelihood estimate (blue lines). The top right panel in Fig. 5 compares the distribution of filament widths from Fig. 3 (histogram) to the functional form of equation 2 with values for the parameters drawn randomly from the posterior distribution of model parameters (smooth line). For the range of parameters used, the shape of the smooth curve varies very little (the variation is similar to the width of the plotted line). The model captures well the basic shape of the distribution and of the model parameter space.

For values of the parameters within 5σ of the mean of their corresponding distributions, we obtain from equation 3: $\langle W\rangle = 0.09 - 0.1$ pc. We conclude that the model used here accurately reproduces the position of the peak of the distribution of widths of Fig. 3 (within 0.01 pc). From the value of σ we obtain a handle on the error introduced by the width calculation algorithm. Since the resolution is only 0.013 pc, the algorithm is the main source of measurement error.

The question that remains to be answered is what determines W_{min}, the value below which the power law distribution is truncated. One obvious culprit could be the resolution limit. However, if W_{min} were equal to the telescope beam size (0.013 pc, shown by the vertical dashed line in Fig. 4), the mean of the distribution would fall below 0.03 pc, as seen from Fig. 4. Another possibility would be that the combined effect of the telescope resolution and the errors of the width-measurement algorithm are setting the lower limit. This corresponds to the parameter σ which is almost 3 times the beam size (for the distribution of widths in Fig. 3). W_{min}, however, is found to be almost 6 times the beam size, making both options unlikely.

A more likely possibility is that W_{min} is related to the range over which the Gaussian fit is performed to measure the width of a profile. In order to avoid fitting the wings of filament profiles, studies of filament widths have chosen to fit a Gaussian within a range of $\sim$ 0.1 to 0.4 pc from the

Table 2. Values of the parameters returned by the MLE for distributions with different initial fitting ranges. The final column shows the values derived from the parameters using equation 3.

Fitting range (pc)	σ (pc)	γ	W_{min} (pc)	$\langle W \rangle$ (pc)
0.04	0.012	4.65	0.037	0.05
0.06	0.019	3.97	0.049	0.07
0.08	0.027	4.13	0.064	0.08
0.10	0.036	4.07	0.074	0.10
0.12	0.043	4.25	0.087	0.11
0.14	0.051	4.16	0.094	0.12
0.20	0.065	3.24	0.110	0.16
0.25	0.079	3.03	0.125	0.19

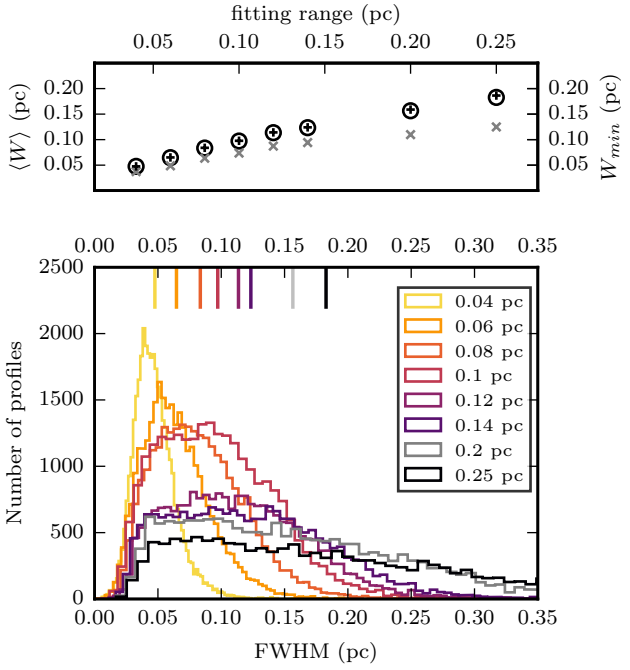

Figure 6. Top: the mean of the observed distributions (open circles) and that calculated from equation 3 (crosses) with the MLE values of the parameters, versus the fitting range (left vertical axis). Values of W_{min} returned by the MLE for each distribution as a function of fitting range are shown as grey crosses (right vertical axis). Bottom: Distributions of beam-deconvolved profile widths in the Polaris Flare for different values of initial fitting range (distance from the axis of a filament). The vertical lines at the top show the mean value of each distribution.

filament spine (Arzoumanian et al. 2011; Juvela et al. 2012; Smith, Glover & Klessen 2014; Koch & Rosolowsky 2015; André et al. 2016; Federrath 2016). However, Smith, Glover & Klessen (2014) have shown that the selection of fitting range drastically affects the mean filament width.

We investigate this effect further for the filaments in the Polaris Flare, by creating distributions of widths with different initial fitting ranges, and repeating the MLE analysis for each one. The resulting values of the parameters are listed in Table 2. As can be seen in Fig. 6, the peak of the distribution of widths shifts towards lower values for smaller fitting ranges (vertical line segments on the top of the main panel). From the top panel of Fig. 6 (left vertical axis), we find that the mean of the observed distributions (open circles) is in very good agreement with the mean calculated with equation 3 using the values of Table 2 (black crosses). Both quantities increase monotonically with the fitting range. This is because W_{min} also has such a dependence on the fitting range (Fig. 6 top panel, right vertical axis). *Since the fitting range used in previous studies does not vary much, it is not surprising that the peak of the filament-averaged width distribution is found at similar values for different clouds.*

Compared to the simulations of Smith, Glover & Klessen (2014), the mean width of filaments in the Polaris Flare increases slightly more abruptly as a function of fitting range. For a factor of ~ 3 increase in fitting range, these authors find the mean width to increase by a factor of 1.5, whereas we find a factor of ~ 2. However, any such comparison must consider the range that we use as an upper limit, because we fit Gaussians iteratively beginning from the quoted fitting range. Also, there is an indication in Fig. 6 that at larger ranges the slope tends to flatten out. Considering these factors, we find the scaling of mean width with fitting range to be strikingly similar between the simulated and observed filaments, perhaps hinting at common structural properties.

The dependence of the mean width on the fitting range suggests that selecting a scale over which to observe/measure a structure determines how important the inner-most part of the structure will appear[4]. In the case of a scale-free structure this can be understood, as a fractal surface changes in character when examined at different scales: it appears smoother/flatter when observed from further away, but upon closer inspection substructure appears. Alternatively, for a structure with a well-defined peak, a Gaussian fit with offset will always return a narrower FWHM for a smaller fitting range.

4 SUMMARY

In this work we have explored the analysis of filament widths in an attempt to find a way to reconcile the proposed "characteristic" width of filaments with the absence of its imprint in spatial power spectra. Our findings can be summarized in the following points:

i. The selected methodology for measuring widths can produce a peaked distribution even if the original data do not contain a preferred scale.
ii. The process of averaging over filament profiles results in a distribution that is necessarily narrow, as a result of the central limit theorem.
iii. Widths vary significantly as a function of position on the spine of a filament.

[4] Observational evidence for substructure in *Herschel* filaments (through finer resolution imaging) already exists, see e.g. Fernández-López et al. (2014); Henshaw et al. (2016, 2017).

iv. The position of the previously identified peak (0.1 pc) in *Herschel* data could be determined by the choice of distance from the filament spine within which the width is measured.

The above suggests that filaments are unlikely to have a constant width, a result which explains the lack of a characteristic scale in the spatial power spectrum of the Polaris Flare. Finally, we note that our results are specific for the widths of filaments and do not contradict the (well-established) existence of other typical length scales in clouds (Mouschovias 1991).

ACKNOWLEDGEMENTS

We would like to thank Dmitriy Blinov, Vasiliki Pavlidou, and Aris Tritsis for fruitful discussions as well as Vassilis Charmandaris, Paul Goldsmith, Nick Kylafis, and Josh Peek for their helpful comments on the paper. We are grateful to the anonymous reviewer for a detailed report which greatly improved this work. Also, we thank Monica He for her contribution during the first steps of this work and Damianos Mylonakis for helping out with technical issues. We used the python module `corner` (Foreman-Mackey 2016) to produce Fig. 5. This research made use of Astropy, a community-developed core Python package for Astronomy (Robitaille et al. 2013). G.V.P. and K.T. acknowledge support by FP7 through the Marie Curie Career Integration Grant PCIG-GA-2011-293531 "SFOnset" and partial support from the EU FP7 Grant PIRSES-GA-2012-31578 "EuroCal". J. J. A. acknowledges funding from the European Research Council under the European Union's Seventh Framework Programme (FP/2007-2013)/ERC Grant Agreement n. 617001.

This research has used data from the *Herschel* Gould Belt Survey (HGBS) project (`http://gouldbelt-herschel.cea.fr`). The HGBS is a *Herschel* Key Programme jointly carried out by SPIRE Specialist Astronomy Group 3 (SAG 3), scientists of several institutes in the PACS Consortium (CEA Saclay, INAF-IFSI Rome and INAF- Arcetri, KU Leuven, MPIA Heidelberg), and scientists of the *Herschel* Science Center (HSC).

REFERENCES

André P. et al., 2010, A&A, 518, L102
André P., Di Francesco J., Ward-Thompson D., Inutsuka S.-I., Pudritz R. E., Pineda J. E, 2014, Protostars and Planets VI, 27
André P. et al., 2016, A&A, 592, 54A
Arzoumanian D. et al., 2011, A&A, 529, L6A
Alves de Oliveira C., 2014, A&A, 568, 98A
Auddy S., Basu, S., Kudoh, T., 2016, ApJ submitted, arXiv: 1609.02989
Benedettini M. et al., 2015, MNRAS, 453, 2036B
Brockwell P. J., Davis R. A., 2002, in Casella G., Fienberg S., Olkin I., eds, Introduction to time series and forecasting. Springer-Verlag, New York, p. 19, 55, 94-95
Elia D. et al., 2014, ApJ, 788, 14
Elmegreen B. G., Falgarone E., 1996, ApJ, 471, 816
Elmegreen B. G., Scalo J., 2004, ARA&A, 42, 211
Federrath C., 2016, MNRAS, 457, 375
Fernández-López M. et al., 2014, ApJ, 790L, 19F
Fischera J., Martin P. G., 2012, A&A, 547, A86
Foreman-Mackey D., Hogg D. W., Lang D. Goodman J., 2013, PASP, 125, 306F
Foreman-Mackey D., 2016, JOSS, 1, 2
Goodman A. A., Barranco J. A., Wilner D. J., Heyer M. H., 1998, ApJ, 504, 223
Hartmann L., 2002, ApJ, 578, 914
Heithausen A., 2002, A&A, 393, 41
Heitsch F., 2013, ApJ, 769, 115
Hennebelle P., 2013, A&A, 556, A153
Hennebelle P., André P., A&A, 560, A68
Henshaw J. D., Caselli P., Fontani F., Jimenez-Serra I., Tan J. C., Longmore S. N., Pineda J. E., Parker R. J., Barnes A. T., 2016a, MNRAS, 463, 146
Henshaw J. D., Jimenez-Serra I., Longmore S. N., Caselli P., Pineda J. E., Avison A., Barnes A. T., Tan J. C., Fontani F., 2017, MNRAS, 464L, 31H
Juvela M. et al., 2012, A&A, 541, A12
Koch E. W., Rosolowsky E. W., 2015, MNRAS, 452, 3435
Koen C., Kondlo L., 2009, MNRAS, 397, 495
Könyves V. et al., 2015, A&A, 584, 91
Malinen J., Juvela M., Rawlings M. G., Ward-Thompson D., Palmeirim P., André P., 2012, A&A, 544, A50
Miville-Deschênes M.-A. et al., 2010, A&A, 518, L104
Miville-Deschênes M.-A., Duc P.-A., Marleau F., Cuillandre J.-C., Didelon P., Gwyn S., Karabal E., 2016, A&A, 593, 4M
Mouschovias T. Ch., 1991, ApJ, 373, 169
Musgrave K., Kolb C. E., Mace R. S., 1989, Computer Graphics, 23, 41
Ntormousi E., Hennebelle P., André P., Masson J., 2016, A&A, 589, 24N
Panopoulou G. V., Psaradaki I., Tassis K., 2016, MNRAS, 462, 1517P
Panopoulou G. V., Tassis K., Goldsmith P. F., Heyer M., 2014, MNRAS, 444, 2507P
Perlin K., 1985, Computer Graphics, 19, 287
Pingel N. M. et al., 2013, ApJ, 779, 36P
Planck Collaboration, 2016, A&A, 586, A138
Polychroni D. et al., 2013, ApJL, 777, L33
Robitaille T. P. et al., Astropy Collaboration, 2013, A&A, 558, A33
Stutzki J., Bensch F., Heithausen A., Ossenkopf V., Zielinsky M., 1998, A&A, 336, 697
Smith R. J., Glover S. C. O., Klessen, R. S., 2014, MNRAS, 445, 2900S
Sousbie T., 2011, MNRAS, 414, 350
Tassis K., 2007, MNRAS, 382, 1317
Wagle G. A., Troland T. H., Ferland G. J., Abel N. P., 2015, ApJ, 809, 17W
Ward-Thompson D. et al., 2010, A&A, 518, L92

APPENDIX A: `DISPERSE` SKELETONS OF HERSCHEL IMAGES

As explained in section 2, the first step in the analysis of filament widths is the identification of the filaments in the image. This is done here by using `DISPERSE` (Sousbie 2011) to acquire the skeleton of the image and then using `FILTER` (Panopoulou et al. 2014) to post-process the skeleton and discard spurious structures.

The (post-processed) skeletons of the three clouds (Polaris Flare, Aquila and IC 5146) used in our analysis are shown in Figs. A1 − A3 (coloured lines) overplotted on the 250 μm *Herschel* images. Each line represents a single structure (filament). The parameters of `DISPERSE` for these skeletons are shown in table A1. The skeletons obtained are very

Table A1. Parameters of DISPERSE used for the skeletons of Fig. A1 − Fig. A3.

Cloud	persistence (MJy/sr)	robustness (MJy/sr)	smooth	assemble (degrees)
Polaris Flare	15	16	50	60
Aquila	80	82	50	50
IC 5146 1	400	410	60	90
IC 5146 2	50	51	100	60
IC 5146 3	40	55	100	40

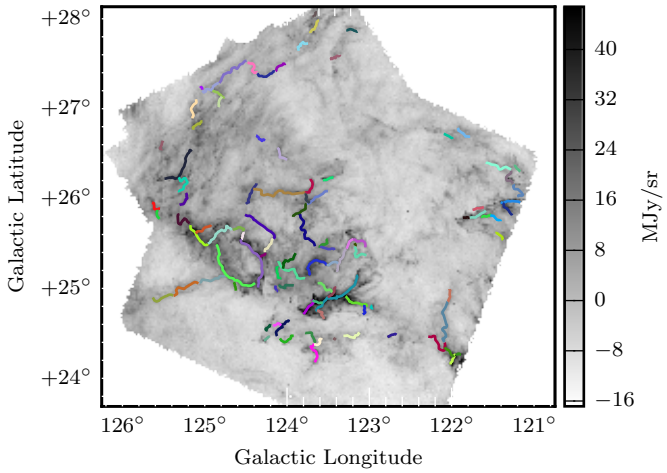

Figure A1. Skeleton of the Polaris Flare 250 μm *Herschel* image constructed with DISPERSE and post-processed with FILTER. Coloured lines trace the spines of filaments used in our analysis.

similar to those of Arzoumanian et al. (2011); Könyves et al. (2015); André et al. (2014).

For the Polaris Flare and Aquila, DISPERSE was run directly on the entire (unfiltered) *Herschel* image. The skeleton for IC 5146 was produced by running DISPERSE on three sub-maps (divided by grey lines in Fig. A3) and combining the resulting skeletons. This enabled us to isolate regions of similar intensity, as in the whole map the differences in brightness caused either faint structures not to be identified or spurious structures to be identified in the brightest parts. In table A1, indices 1, 2, and 3 refer to the left, middle and bottom regions of the map respectively.

We have performed a parameter study for the skeletons of the image of Aquila to test for effects on the distribution of filament profile widths. The ranges of parameters used (for parameter definitions see Sousbie 2011) were: persistence 60 − 80 MJy/sr, robustness 82 − 102 MJy/sr, smoothing 50 − 200, and assembling of arcs 50 − 90 degrees. All resulting distributions of profile widths were identical.

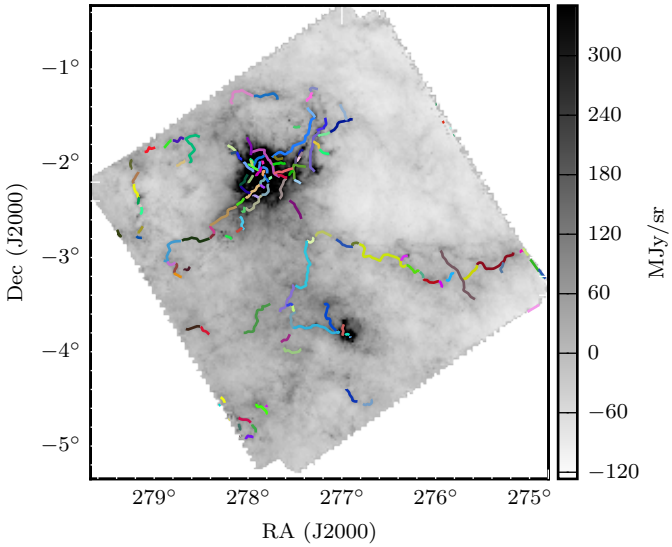

Figure A2. Same as Fig. A1 but for the image of Aquila.

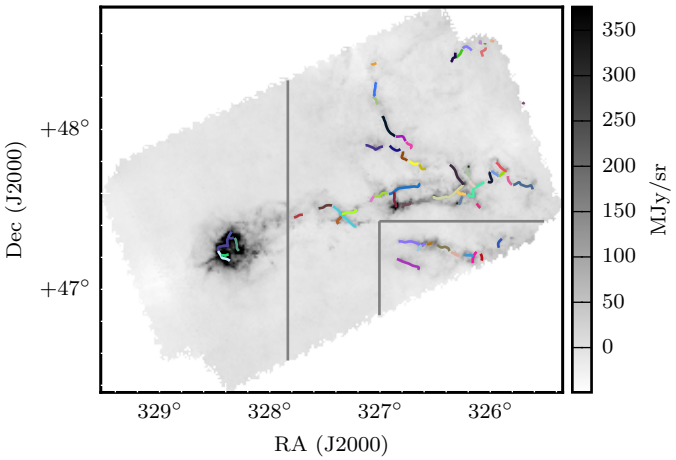

Figure A3. Same as Fig. A1 but for the image of IC 5146. The grey lines divide the image into three submaps on which DISPERSE was run separately.

APPENDIX B: CAN A CHARACTERISTIC SCALE BE 'HIDDEN' FROM THE POWER SPECTRUM?

In this section we use simple artificial images to investigate the effect of a characteristic scale on the azimuthally averaged spatial power spectrum of an image.

Our tests consist in creating elongated structures with radial profiles following the form of a Plummer profile in column density (a form which fits well the column density profiles of observed filaments, Arzoumanian et al. 2011). The

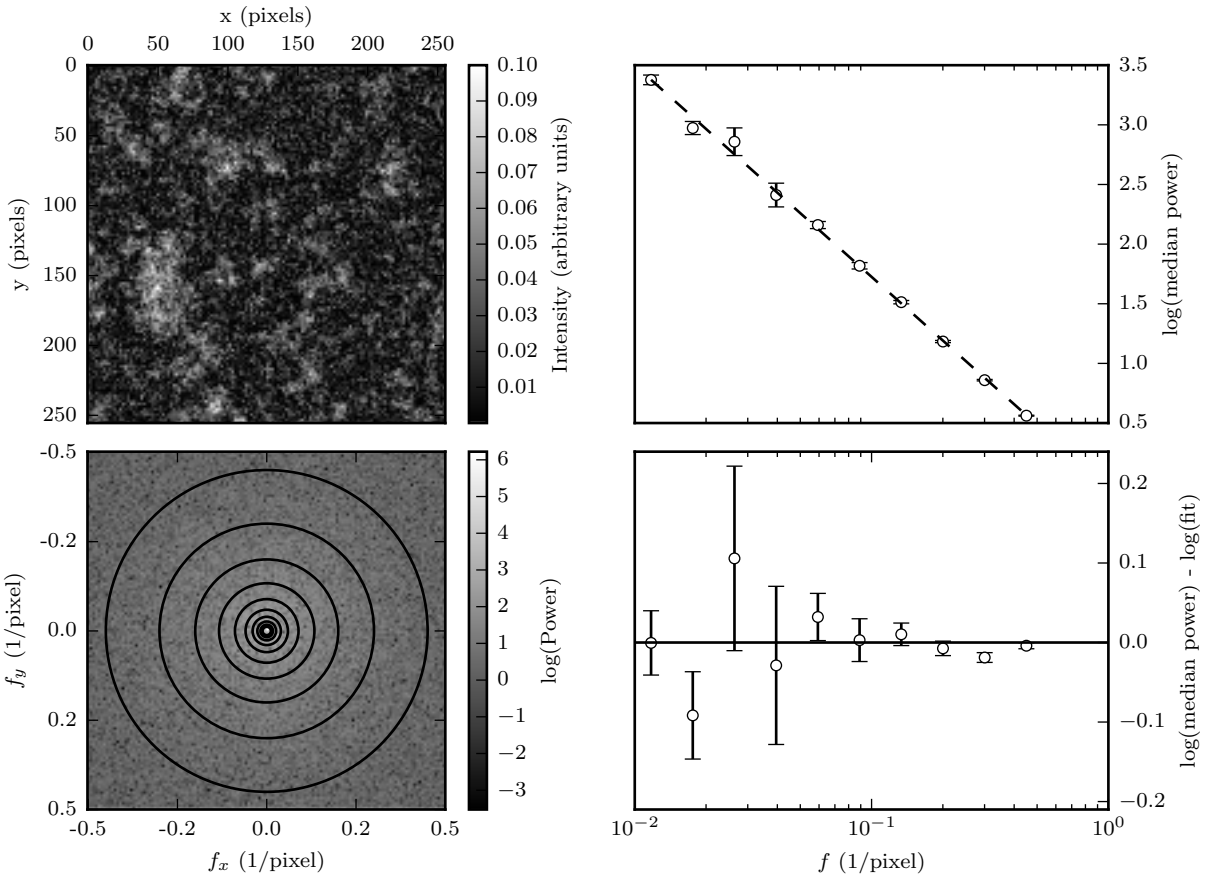

Figure B1. Top left: two-dimensional pink noise that is used in subsequent images of artificial filaments. Bottom left: two-dimensional spatial power spectrum of the image with annuli drawn to indicate the regions within which the azimuthally-averaged power spectrum (top right) is calculated. Top right: Azimuthally averaged spatial power spectrum with errors and linear fit performed in log-log space (dashed line). Bottom right: Difference between the (logarithms of the) spatial power spectrum and the fit.

intensity of the profile of an artificial filament is I_0 on its spine, has an inner flat portion (in logarithmic space) of size R_{flat}, and drops with distance (r) from the axis of the filament as:

$$I(r) = \frac{I_0}{[1 + (r/R_{flat})^2]^{\frac{p-1}{2}}}. \quad \text{(B1)}$$

For the exponent, p, we choose a value of $p = 2$, as observed for filaments in *Herschel* data (Arzoumanian et al. 2011)

The artificial filaments have very simplistic characteristics: they are straight, have a constant peak intensity along their spine, and a constant R_{flat}. This should make the identification of the signature of any characteristic scale (width, length), in the spatial power spectrum, unambiguous. In this section we use R_{flat} as a proxy of the width of the artificial filaments as for profiles with $p = 2$, FWHM $\approx 3R_{flat}$ (Arzoumanian et al. 2011).

The filament images are co-added with (the same) two-dimensional isotropic pink noise. We generate the noise by creating the coefficients of its two-dimensional Fourier transform. Each coefficient C_k has a magnitude of $1/\sqrt{k_x^2 + k_y^2}$ and a random phase (C_0 is set to 0). We obtain the final pink noise image by applying the inverse Fourier transform (Fig. B1, top left). Its two-dimensional power spectrum is shown in the bottom left panel. The azimuthally-averaged power spectrum (constructed by taking the median power within the annuli drawn on the two-dimensional power spectrum, as in Pingel et al. 2013) has the form of a power-law (Fig. B1, top right). The deviation from a perfect power-law can be quantified by the residuals of the power spectrum from a linear fit in log-log space (dashed line in top right panel). From the bottom right panel of Fig. B1 we see that the level of the residuals, log(median power) - log(fit), is less than 0.2. As in section 3.1, the error of the median of each annulus is quantified by bootstrap resampling the distribution of intensities within the annulus.

Fig. B2 (left) shows a single filament that has $R_{flat} = 8$ pixels and is 80 pixels long. The spatial power spectrum of the image (top right) has been fit by a line. The power spectrum deviates significantly from this line at the spatial frequencies corresponding to R_{flat} (dashed vertical line) and the filament's length (dotted vertical line) as can be seen in the bottom left panel of the figure.

In Fig. B3, we investigate the effect of changing the

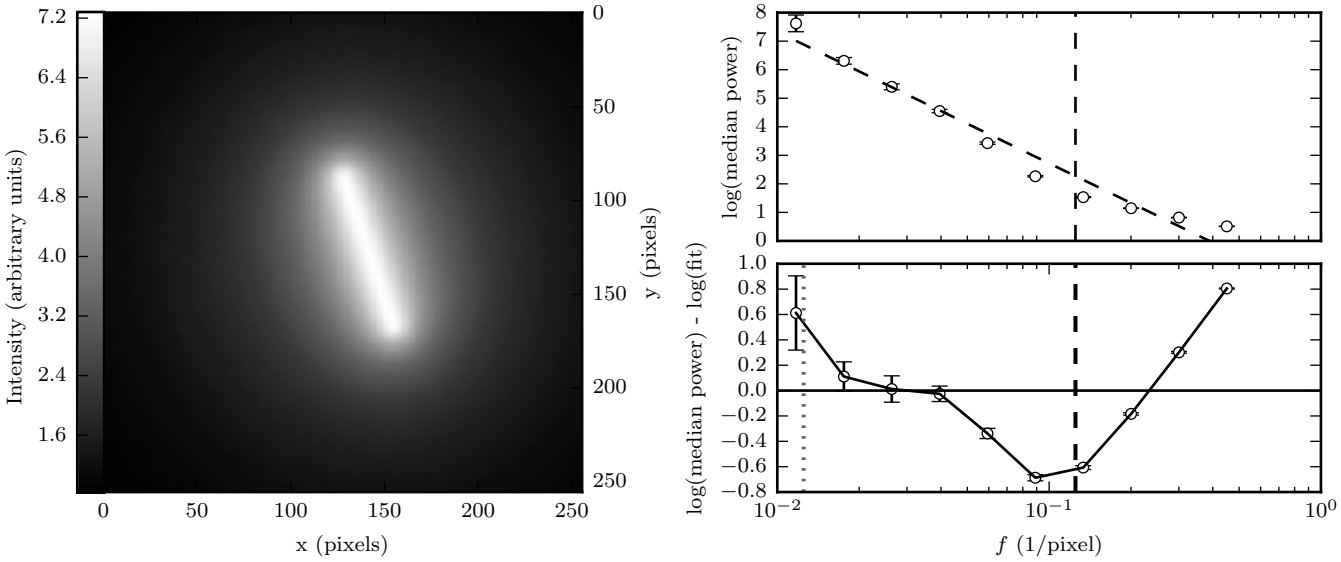

Figure B2. Left: Artificial image of a single filament with $R_{flat} = 8$ pixels and length = 80 pixels. Top right: spatial power spectrum of the image with a linear fit in log-log space (dashed line). Bottom right: difference between the (logarithms of the) power spectrum and fit. The dashed vertical line shows the spatial scale corresponding to the width R_{flat}, while the dotted line shows the scale corresponding to the length. Low intensity pink noise (Fig B1) has been added to the image of the filament.

width (R_{flat}) of this single filament. As R_{flat} changes from 8 (top) to 12 (middle) and finally to 16 (bottom) pixels, the signature of this scale on the power spectrum moves to the corresponding spatial frequencies (indicated by vertical dashed lines).

Having identified the signature of a characteristic scale on the power spectrum, we now investigate the circumstances under which it may be possible to 'hide' such a signature in a way that it does not appear in the power spectrum. We first create a map with 10 filaments of the same length (40 pixels) but with random orientations and positions. Each filament has a different peak intensity and R_{flat} (constant along its spine). The R_{flat} are drawn from the narrow distribution of mean filament widths found in Fig. 2 (bottom panel). The values drawn from this distribution were multiplied by 100 to obtain R_{flat}, meaning that a value of 0.1 pc is mapped to 10 pixels (a scale that is well-sampled in the power spectra of the artificial images). The image is shown in Fig. B4, with each of the vertical dashed lines denoting the spatial frequency that corresponds to $1/R_{flat}$ for the 10 filaments. Even when multiple filaments are present, with random orientations and spacings between them, the signatures of their characteristic scales are clearly visible as deviations from the fit to the power spectrum. These deviations are significantly larger than those seen in the power spectrum of the pink noise.

We investigate the statistical significance of this result by creating 150 realizations of such images. We find that in only $\sim 10\%$ of the images, the maximum residual of the fit is less than 0.2 in amplitude (in the range of frequencies corresponding to the values of R_{flat}). However, upon visual inspection, these images can be divided into three categories: (i) the residuals exhibit a systematic offset from the fit, but at a level less than 0.2, (ii) only a single point in the power spectrum samples the range of scales used, or (iii) most filaments overlap at a certain part of the image, so their individual filamentary structure is not visible. In the first case, the systematic offset of neighbouring data points is distinct from the random fluctuation of the residuals in the pink noise image. Thus, a signature of the width is still identifiable in the spatial power spectrum. In the second case, an offset is observed at data points outside but neighbouring to the range considered. In the last case, the imprint of the larger 'cluster' dominates the power spectrum and these images cannot be considered as being comprised of filaments.

Finally, we introduce pink noise with very large amplitude (maximum intensity $\sim$30% that of the largest filament spine intensity) in Fig. B5. The filaments in this image are the same as in Fig. B4. Now, the signature of the width (a change of the spectral slope at the corresponding spatial frequency range) is not visible in the residuals of the power spectrum from the fit. However, the filaments are barely distinguishable from the background noise, which is in stark contrast to observations of clouds.

We conclude that the existence of a characteristic scale should appear in the spatial power spectrum of an image (e.g. as a change in the spectral slope), provided that the structure is easily discernible from the background. In the case of the spatial power spectrum of the Polaris Flare (Miville-Deschênes et al. 2010), no such change exists in the power spectrum at or near the spatial scale corresponding to the "characteristic" width (of the very prominent filaments) at 0.1 pc.

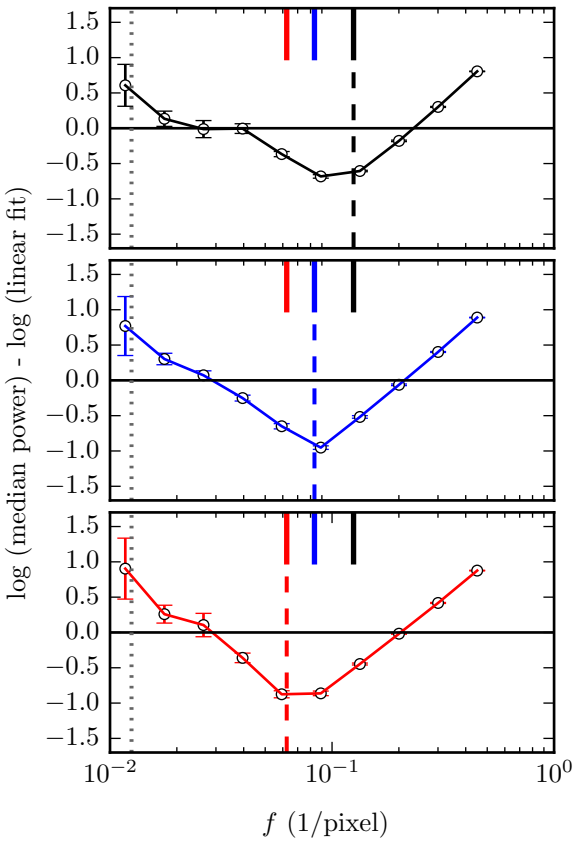

Figure B3. Difference between the spatial power spectrum and a linear fit in log-log space (log(median power) - log(fit)) for an artificial image with a single filament of constant R_{flat}. From top to bottom: $R_{flat} = 8, 12, 16$ pixels. The length is 80 pixels for all three images (dotted vertical line). In each plot, the dashed vertical line shows the spatial frequency that corresponds to R_{flat}. The small vertical lines on the top of each panel show the values of R_{flat}^{-1} of all 3 images, for comparison between panels.

APPENDIX C: ARMA MODELLING OF FILAMENT WIDTHS

In section 3.2 we saw that the distributions of all profile widths and of filament lengths are necessary but not sufficient pieces of information to explain the spread of the distribution of mean filament widths (σ_{mean}). The goal of this section is to model the variation of widths along the ridge of a filament. Using this information, we will be able to explain quantitatively how one obtains a distribution with σ_{mean} when averaging the widths from the parent distribution of all profile widths.

We choose to model the variation of profile widths along a filament using an Auto-Regressive-Moving-Average (ARMA) process (for a complete description of ARMA modelling, we refer the reader to Brockwell & Davis 2002). Each filament is regarded as a series of N widths, w_i, measured at all positions (pixels), $i = 1-N$, along the filament crest. The difference between the width at point i along the filament crest and the mean width can be written as the regression:

$$\delta w_i = \alpha_0 \delta w_{i-1} + \alpha_1 \delta w_{i-2} + \alpha_2 \delta w_{i-3} + ... + \epsilon_i + c_1 \epsilon_{i-1} + ... \quad \text{(C1)}$$

where δw_{i-1} is the difference of the width of the point previous to i from the mean width, δw_{i-2} is measured two points away, and so on. Depending on the order p of the auto-regressive (AR) part of the equation (coefficients α), δw_i can have a dependence on the width measured p points away from position i. ϵ_i is the residual, what is not taken into account by the AR terms. It is assumed random and normally-distributed. The terms containing the residuals at different positions are the moving-average terms (MA) and their number q is the order of the MA part of the model.

We wish to model the variation of widths along a filament, based on the data in the Polaris Flare. In order to find an appropriate model, we must first decide on the order of the model to be fit. The order of the ARMA model (p, q) can be determined by examination of the Autocorrelation and Partial Autocorrelation functions (ACF, PACF) of the widths of filaments in the Polaris Flare for p and q, respectively (Brockwell & Davis 2002).

The ACF is defined as (following Brockwell & Davis 2002):

$$\mathrm{ACF}(l) = \frac{1}{N\sigma_{fil}^2} \sum_{i=1}^{N-l} (w_{i+l} - \langle w \rangle)(w_i - \langle w \rangle),\ 0 < l < N \quad \text{(C2)}$$

where N is the number of profiles in a filament, l is the distance (lag) measured along the filament ridge, w_i is the width of the i^{th} profile along the ridge and $\langle w \rangle$ is the average width of the filament. Finally, σ_{fil} is the standard deviation of profile widths in the filament. The PACF at a given lag is the autocorrelation at this lag after removal of an AR model of order lag minus 1. This means that the PACF will be zero at this lag if the AR model effectively removes all correlation.

Fig. C1 shows the ACF of widths of all filaments in the Polaris Flare versus distance along the filament ridge[5]. The ACF drops abruptly and stays around zero for distances larger than approximately twice the beam size (HPBW = 0.013 pc, dashed vertical line). For most filaments, widths are strongly correlated only within the beam size. This corresponds to a lag of 3 pixels, and therefore this is the order of the AR process ($p = 3$). The ACF of filaments in IC 5146 and Aquila also follow this trend (for IC 5146 HPBW = 0.04 pc, and for Aquila HPBW = 0.023 pc). In Fig. C2 we plot the PACF of all filaments in the Polaris Flare versus the lag in pc. The PACF (averaged over all filaments for every given lag) drops after a lag of 0.004 pc (1 pixel).

Therefore, the (mean-subtracted) widths along filaments in the Polaris Flare can be modelled with $p = 3$ AR terms and $q = 1$ MA term:

$$\delta w_i = \alpha_0 \delta w_{i-1} + \alpha_1 \delta w_{i-2} + \alpha_2 \delta w_{i-3} + \epsilon_i + c_1 \epsilon_{i-1}. \quad \text{(C3)}$$

We fit equation C3 to the series of widths of each filament in the Polaris Flare. We wish to obtain a single model that

[5] For ARMA modelling and for construction of the ACF we made use of the python module `statsmodels` (`http://statsmodels.sourceforge.net/`)

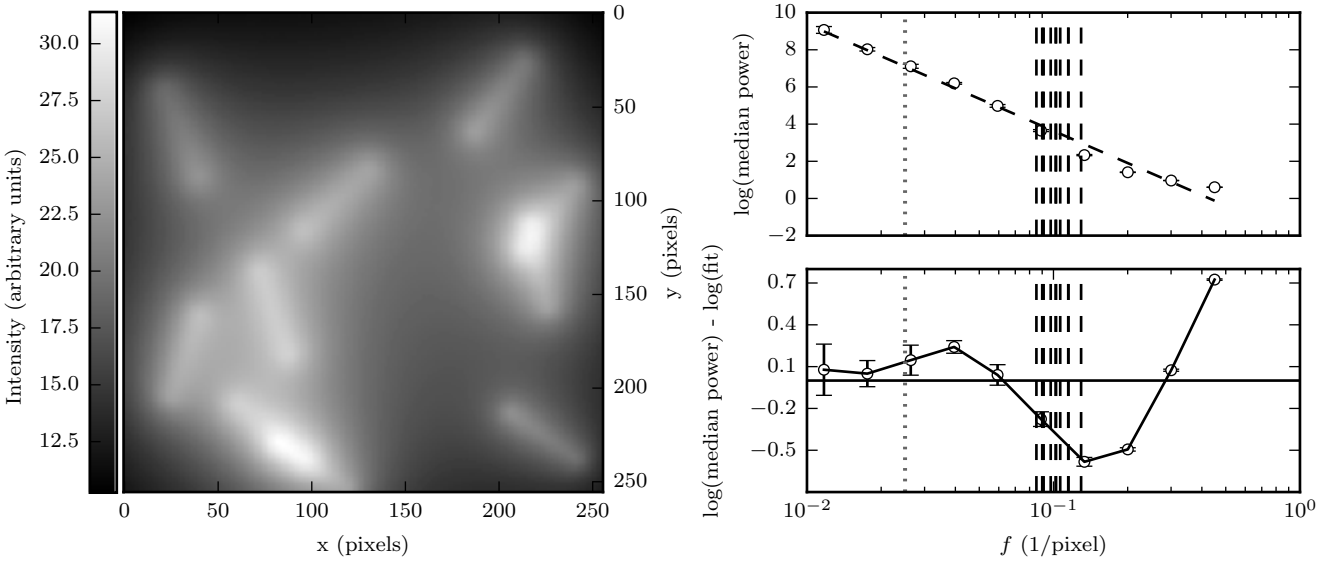

Figure B4. Same as Fig. B2 but for 10 filaments at random orientations, with a length of 40 pixels and different R_{flat}, drawn from the distribution of mean filament widths in Fig. 2 (with values multiplied by 100 so that 0.1 pc is mapped to 10 pixels). The spatial frequency corresponding to the R_{flat} of each of the filaments is shown with a dashed vertical line.

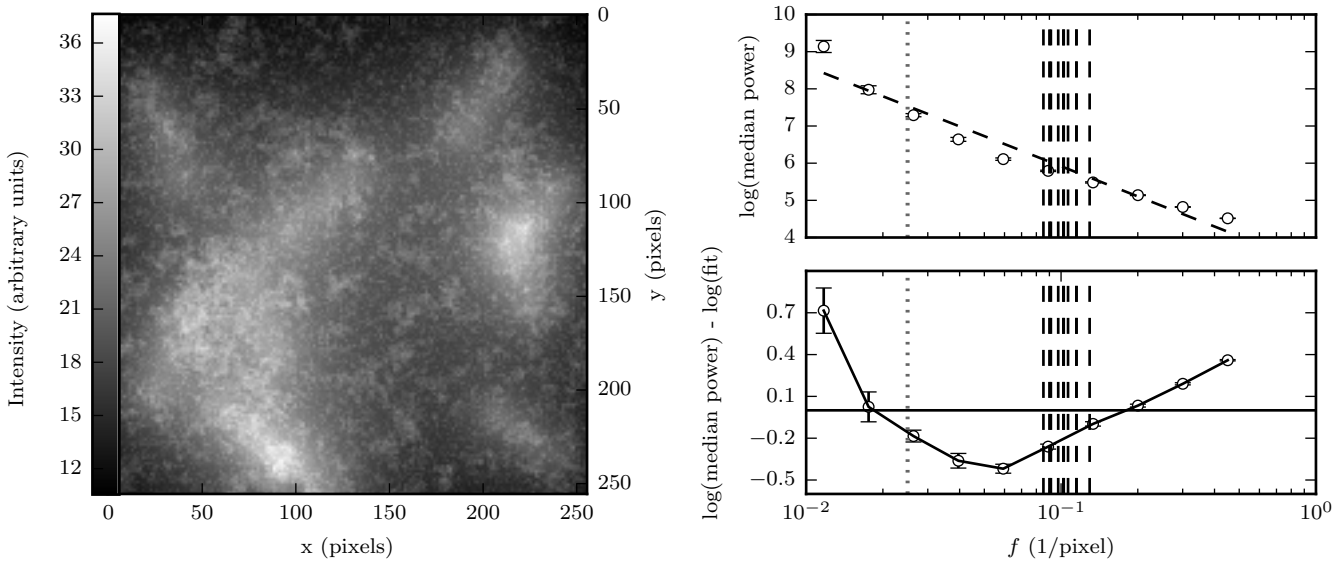

Figure B5. Same as Fig. B4 but with pink noise with maximum intensity $\sim 30\%$ that of the highest filament peak.

on average reproduces well the variation of widths along any filament in the cloud. This model is equation C3 where the value of each coefficient is equal to the median of values returned by fitting the equation to each filament. The median values of the coefficients from the fits to individual filaments are $\alpha_1 = 0.8$, $\alpha_2 = 0.2$, $\alpha_3 = 0.05$, $c_1 = -0.23$.

As seen in section 3.2, the observed σ_{mean} cannot be explained by only taking into account the distributions of all profile widths and filament lengths. We will now estimate what part of σ_{mean} can be attributed to the combined contribution of the correlation between the widths of neighbouring profiles, and the distribution of filament lengths. We note that the information on the distribution of all profile widths is included in the ARMA model, as the coefficients were found by fitting to real data.

To this end, we create 100 groups (filaments) of (mean-subtracted) widths in the following way. A number of profiles for each filament is drawn from the distribution of fila-

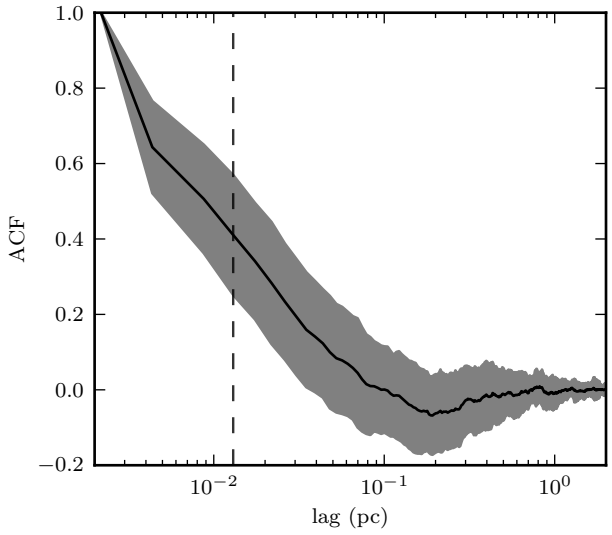

Figure C1. ACF of all filaments in the Polaris Flare versus distance. The black line shows the ACF averaged over all filaments for a given lag (distance). The ±1 standard deviation of the ACF of all filaments at a given lag is shown with a grey band. The vertical line shows the HPBW (beam size) of 0.013 pc. The plot has been truncated at a distance of 2 pc for clarity.

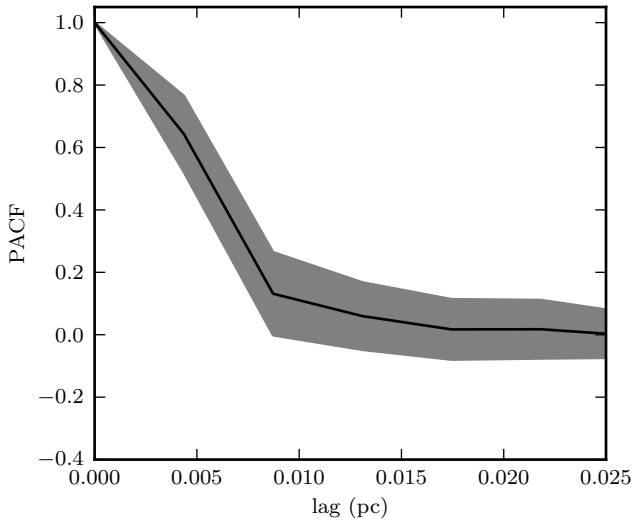

Figure C2. As in Fig. C1 but now showing the PACF of all filaments versus distance. The horizontal axis has been truncated at a distance of 0.025 pc.

ment lengths in the Polaris Flare. Each filament is assigned a starting value drawn from a normal distribution with mean 0 and standard deviation equal to that of the distribution of ϵ_i from the fits to individual filaments. This starting value corresponds to the mean-subtracted width of the first filament profile. Consecutive (mean-subtracted) profile widths are found iteratively using equation C3. We then calculate the average width of each filament. The distribution of average filament widths has a spread of 0.011 pc, similar to the observed σ_{mean} of 0.014 pc in the cloud. This process is repeated 100 times to quantify whether the difference (0.014 pc versus 0.011 pc) is significant. We find that the observed σ_{mean} is within the spread of the results of the simulation.

We have found that σ_{mean} can be predicted based on three pieces of information: the distribution of all profile widths, the distribution of filament lengths, and the correlation of widths within a beam size. From the CLT we understand the effect of these three as follows: A broader distribution of all profile widths will increase the uncertainty on the mean (σ_{mean}), as seen in equation 1. From the same equation, it follows that a population of filaments with on average larger lengths will have a smaller σ_{mean}. Finally, we have seen that neglecting the effect of the beam (random draws of the width from the parent distribution) produces a narrow σ_{mean}. The effect of the beam is to introduce a larger uncertainty on the mean, by effectively reducing the number of independent measurements in a single filament.

This paper has been typeset from a TEX/LATEX file prepared by the author.